QUIET DRONES 2026

Delft, 29th June - 1st July 2026

Numerical Noise Prediction of a Tilting Rotor in Forward Flight

Session: UAS/UAM noise modelling 2

Marco Picillo, Politecnico di Torino, Italy, marco.picillo@polito.it
Mattia Barbarino, CIRA, Italy, m.barbarino@cira.it
Francesco Avallone, Politecnico di Torino, Italy, francesco.avallone@polito.it

Abstract

This work investigates the far-field noise generated by a tilting propeller during the transition from axial inflow to crossflow. The analysis is performed using a low-fidelity framework combining a Vortex Particle Method with a time-domain acoustic solver based on the Ffowcs Williams-Hawkings analogy. Fixed tilting angles are first analyzed to assess the influence of the tilt angle and advance ratio on blade loading and noise emission. Increasing the tilt angle leads to asymmetric loading and a redistribution of acoustic energy, with changes in both magnitude and directivity. The dynamic tilting case reveals unsteady effects, which result in significant variations of thrust and torque. These effects are reflected in the far-field noise through transient overshoots and undershoots of the Sound Pressure Level. Spectrogram analysis shows that these features are associated with a time-localized redistribution of acoustic energy.

Keywords: Drones; Noise; Transitional flight.

1. INTRODUCTION

Advanced Air Mobility (AAM) refers to the use of next-generation air transport systems, such as electric Vertical Take-Off and Landing (eVTOL) aircraft and drones, for the movement of passengers and goods. It includes several operational concepts, such as Urban Air Mobility (UAM), which focuses on operations within cities and suburban areas, while Regional Air Mobility (RAM) addresses longer-distance missions using larger and faster vehicles. The rapid development of these concepts in recent years has been largely enabled by advances in VTOL technologies, i.e. vehicles capable of taking off and landing within confined areas (Zhou, Zhao, & Liu, 2020), typically employing distributed propulsion systems.

AAM is expected to play a significant role in shaping future mobility and societal organization. However, its potential advantages, such as lower emissions, improved quality of life, and increased transport efficiency, must be balanced against important challenges, including safety, certification, and public acceptance.

From the perspective of public acceptance, the study of (Hasan, 2018) highlights noise as one of the main factors affecting societal perception of UAM operations. For this reason, a reliable prediction of rotorcraft noise in urban environments is essential. In fact, they are characterized by highly complex flow conditions, including non-uniform inflow (Jamaluddin, Celik, Baskaran, Rezgui, & Azarpeyvand, 2024), gusts (Voropayev et al., 2025), and turbulence (Alì, Piccolo, Zamponi, Ragni, & Avallone, 2026). These effects lead to spatial and temporal variations of the inflow at the rotor disk, which in turn produce significant changes in Sound Pressure Level (SPL) and its radiation pattern (Romani, Grande, Avallone, Ragni, & Casalino, 2022).

Although propeller noise in stationary and axial inflow conditions has been extensively investigated, its prediction for maneuvering rotorcraft is still far from straightforward. In practical applications, VTOL vehicles and drones operate under a wide range of maneuvering conditions, where parameters such as attitude and rotor speed vary in time, in contrast with steady regimes like hover or steady forward flight, where these quantities remain constant. In fact, rotorcraft motion can be viewed as a succession of equilibrium states linked by transitional phases. These maneuvers are inherently unsteady and often aperiodic, introducing noise generation mechanisms that differ significantly from those observed in steady conditions (Bres, Brentner, Perez, & Jones, 2004). The additional noise associated with these transients becomes more relevant as the maneuver duration decreases, and it is characterized by a time-dependent directivity that can deviate significantly from the steady-state cases (Chen, Brentner, Lopes, & Horn, 2006).

A remarkable maneuver in eVTOL and drone operations is represented by the tilting of the propellers. From an aerodynamic point of view, the rotor blades in a tilt-rotor configuration are subjected to a particularly complex flow field during the transition from vertical to forward flight. This phase is characterized by complex aerodynamic interactions that significantly affect the blade loading. As the rotor disk tilts, the incidence of the incoming flow relative to the blades changes, modifying the local inflow conditions along the span of the blades which can affect aerodynamic performance (Zanotti et al., 2024), stability (Ryll, Bülthoff, & Giordano, 2012) and noise (Jamaluddin et al., 2024).

Various numerical and experimental studies have investigated tiltrotor aerodynamics and acoustics; (Jamaluddin et al., 2024) studied the aerodynamic and acoustic behavior of a tiltrotor configuration across different nacelle tilt angles, showing that variations in the inflow structure can have a marked impact on the Overall Sound Pressure Level (OASPL). (Son, Song, Araghizadeh, Myong, & Lee, 2025) conducted a numerical study on the aerodynamics and acoustics of the XV-15 tiltrotor with a coupled mid-fidelity approach, combinining a source-doublet panel method with a Vortex Particle Method (VPM) for the wake evolution, under different tilting configurations.

However, even if a great number of studies addressed the noise generation mechanisms under various conditions, the problem of the noise generation during a dynamic tilting remains only partially explored (Wang, Bi, Wu, & Zhong, 2026). For this reason, the scope of this work is to better understand the unsteady effect of a dynamic tilting and its noise generation mechanism that could significantly differ from quasi-steady analysis.

2. Methodology

In this section, the low-fidelity framework and the numerical setup used for the simulations is presented. A validation of the framework has been already carried out in (Picillo, Barbarino, & Avallone, 2026) for both static and unsteady operating conditions.

Shortly, the low-fidelity framework couples the aerodynamic solver FLOWUnsteady (Alvarez & Ning, 2018), based on the VPM, with an in-house time-domain acoustic solver for tonal noise prediction. An overview of the computational workflow is provided in Figure 1.

Within the *preprocessing* stage, the VTOL setup is defined, including the propeller and wing geometries, together with the maneuver description, which specifies the time-varying flight conditions. These inputs are then provided to the *processing* stage, where the aerodynamic and acoustic solvers are executed.

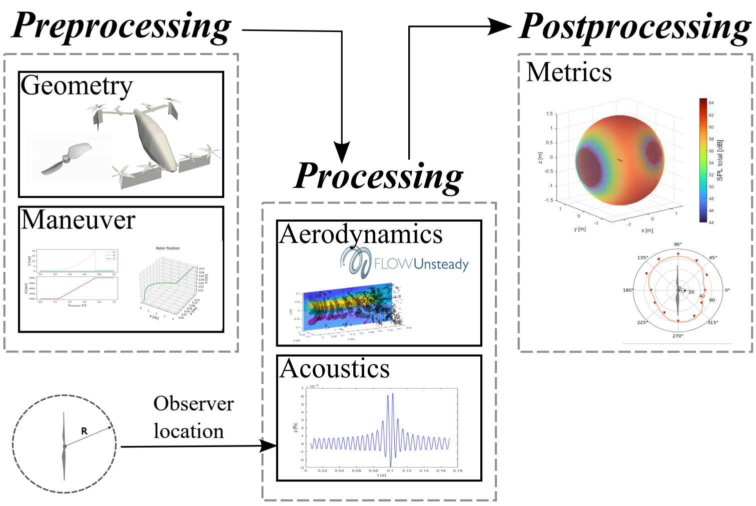

Figure 1: Low-fidelity simulation framework.

FLOWUnsteady relies on a meshless CFD formulation in which the Navier–Stokes equations are solved in the velocity–vorticity form. The flow is represented through a collection of vortex particles, each carrying a localized vorticity distribution described by a radial basis function. Moreover, the blades are discretized into spanwise elements, whose aerodynamic characteristics are defined using two dimensional airfoil data (lift and drag coefficients) obtained from XFOIL. The resulting aerodynamic loads are then fed back into the flow field by translating them into an equivalent vorticity distribution, in accordance with the Kutta-Joukowski theorem.

Furthermore, the aerodynamic solver is based on the FW-H acoustic analogy. The loading noise is evaluated using Farassat's 1A formulation (Brentner & Farassat, 2003), reported in Equation 1, while the thickness noise follows the far-field approximation as proposed in (Glegg & Devenport, 2017) (pp. 415), and presented in Equation 2.

$$
\begin{aligned}
4\pi p'_L(x,t) = & \frac{1}{c_\infty}\int_{f=0}\left[\frac{\dot{\ell}_r}{r|1-M_r|^2}\right]_{\tau=\tau^*} dS \\
& + \int_{f=0}\left[\frac{\ell_r-\ell_M}{r^2|1-M_r|^2}\right]_{\tau=\tau^*} dS \\
& + \frac{1}{c_\infty}\int_{f=0}\left[\frac{\ell_r(r\dot{M}_r+c_\infty M_r-cM^2)}{r^2|1-M_r|^3}\right]_{\tau=\tau^*} dS
\end{aligned} \tag{1}
$$

$$
4\pi p'_T(x,t) \approx \int_{f=0}\left[\frac{\rho_\infty}{r}\frac{\ddot{M}_r}{|1-M_r|^4}+\frac{3\dot{M}_r^2}{|1-M_r|^5}\right]_{\tau=\tau^*} dV \tag{2}
$$

In these equations, ℓ_r is the scalar product between the surface pressure vector and the radiation direction $\hat{r}$, while ℓ_M is its projection along the surface velocity vector normalized by the speed of sound. The overdot indicates differentiation with respect to the emission time. Thinking in terms of forces, the contribution of each blade element *j* is $\mathbf{F} = l\Delta S$ in the global reference frame and $\mathbf{F}_r = l_r\Delta S$ in the radiation direction. The derivative of the force in the radiation direction can be written as:

$$
\dot{\mathbf{F}}_r = \mathbf{F}\cdot\dot{\hat{\mathbf{r}}}+\dot{\mathbf{F}}\cdot\hat{\mathbf{r}} \tag{3}
$$

The integrands in Equation 1 and Equation 2 are evaluated for each blade element at the corresponding retarded time, yielding the pressure signal as a function of observer time for the prescribed rotor motion.

Finally, the propeller used for the simulation is a 2-bladed NACA 4412 with a diameter D_{prop} of 30 cm operating at a constant speed Ω of 6000 rpm. The geometric characteristics of the propeller are shown in Figure 2.

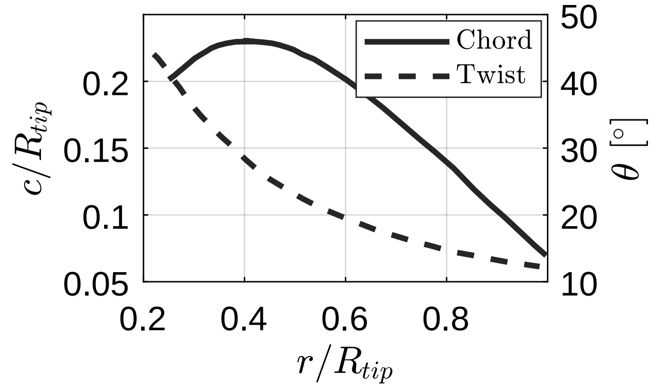

Figure 2: Chord and twist distribution along the radius for the NACA 4412 propeller.

Each blade is then discretized into 25 blade elements equally spaced from the root to the tip.

3. Results

In this section, the results of a tilting propeller in hover and uniform inflow will be described. Firstly, for *tilting* we consider a flight condition in which the propeller changes its attitude, as shown in Figure 3. In particular, during a tilting maneuver, the tilting angle γ changes in time, causing the propeller, in forward flight, to experience a time-varying inflow that affects the aerodynamic performance and the noise generated by the propeller.

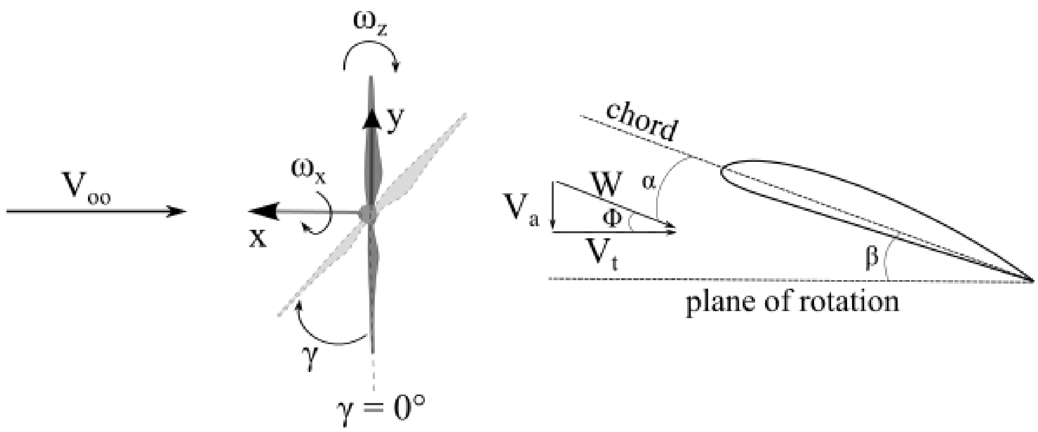

Figure 3: Tilting sketch and schematic of a blade element.

At this stage, a distinction is made between a fixed tilting angle and a dynamic tilting. For the fixed tilting the analysis are performed at different γ angles, with the propeller frozen at that specific condition; while in a dynamic tilting the propeller changes the γ angle in time with a prescribed law. In this way, the fixed tilting angle conditions are used as a reference for specific γ angles during the dynamic maneuver, in order to understand if the tilting could be described as a series of quasi-steady states, or if dynamic phenomena occurs during the transition between an initial and a final condition.

3.1 Fixed tilting angle

The aerodynamic performance, in terms of thrust (C_T) and torque (C_Q) coefficients, defined in Equation 4, and shown in Figure 4 (a,b), are evaluated for different flight conditions, i.e. for different advance ratios (J) and tilting angles (γ), together with their root-mean-square (RMS) values, Figure 4 (c,d), in order to reconstruct a performance map of the propeller.

$$C_T = \frac{T}{\rho_\infty n^2 D_{prop}^4} \qquad C_Q = \frac{Q}{\rho_\infty n^2 D_{prop}^5} \qquad J = \frac{V_\infty}{(\Omega/60) D_{prop}} \tag{4}$$

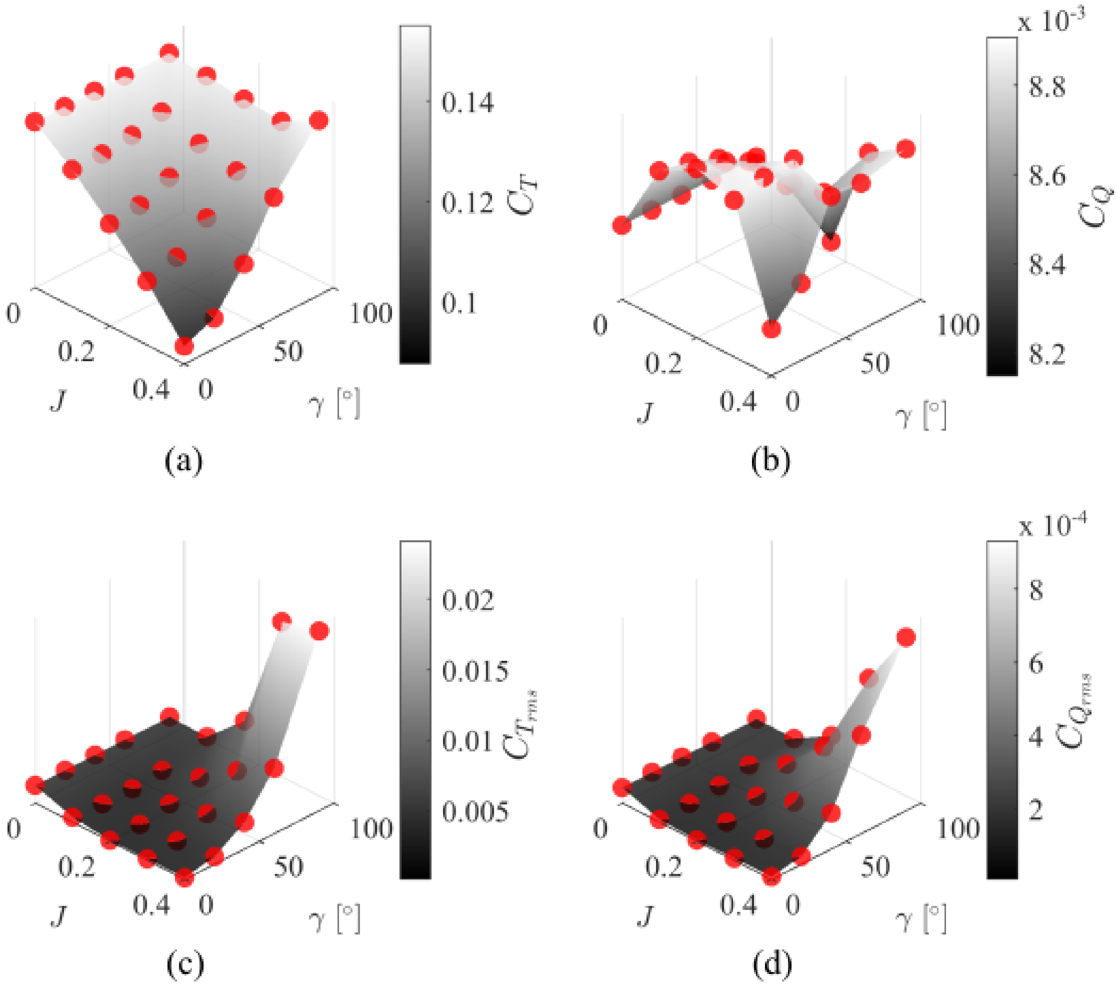

Figure 4: Static aerodynamic performance maps.

As shown in the figure, C_T increases as J decreases, while the effect of the tilt angle γ on the propeller performance becomes more pronounced at higher J values. In contrast, the torque coefficient C_Q does not exhibit a clear or consistent trend across the investigated operating range. However, its RMS values increase with γ for $J > 0$, and with J for $\gamma > 0$, indicating enhanced unsteady effects when both parameters depart from zero.

A relevant reference condition is represented by $\gamma = 0^\circ$, corresponding to a purely axial inflow. As shown in Figure 5, increasing the advance ratio J leads to a faster downstream convection of the propeller wake, accompanied by a reduction in vorticity intensity. This behavior is consistent with the lower effective angle of attack experienced by the blades at higher J, shown in Figure 6 (a). Conversely, at $J = 0$, the wake remains concentrated beneath the rotor disk, resulting in increased unsteady loading of the propeller, Figure 6 (c). Overall, under axial inflow conditions, both the wake structure and the aerodynamic loading along the blades remain axisymmetric with respect to the propeller axis.

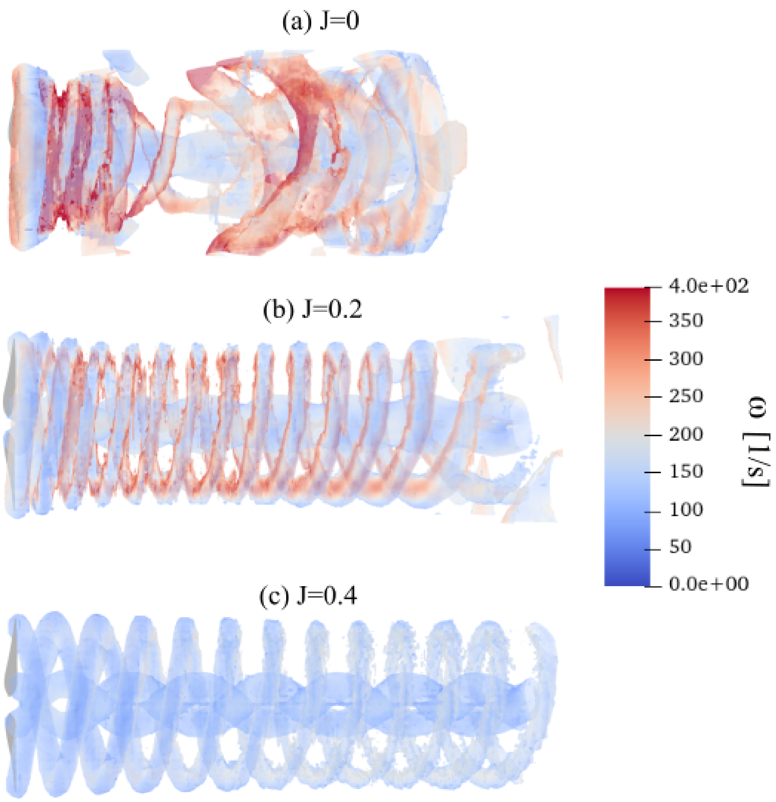

Figure 5: Propeller wake structure for different J and $\gamma = 0°$.

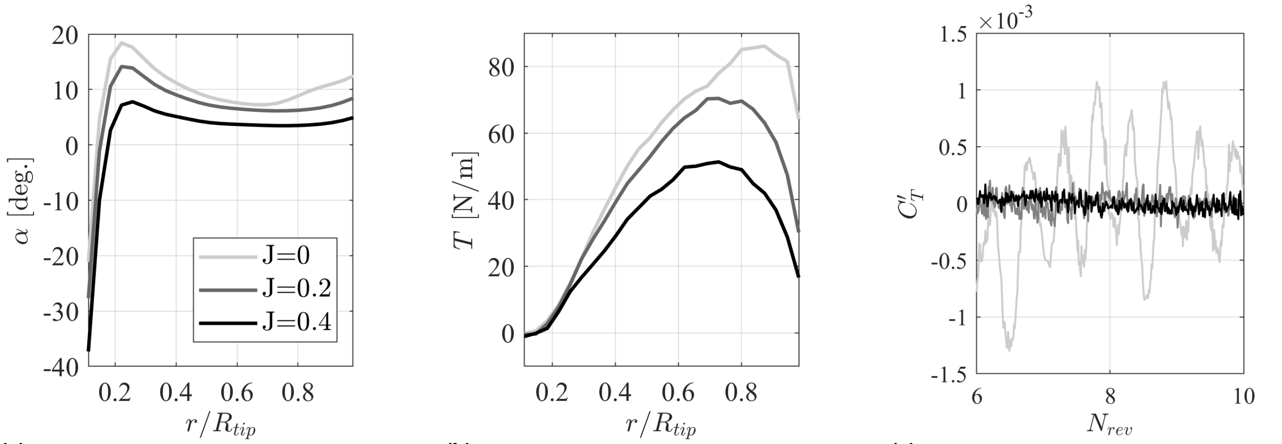

(a) (b) (c)

Figure 6: Radial distribution of angle of attack (a) and thrust (b) along the blade radius; and fluctuating thrust coefficient component (c) at different J and $\gamma = 0°$.

When the propeller is tilted, both the wake and the loading lose their axial symmetry, as evident from Figure 7 and Figure 8. At $\gamma = 40°$, the wake is still mainly helical but skewed, with stronger vorticity on the upper side of the rotor plane.

The thrust distributions in Figure 8 reflect the same behavior. At $\gamma = 40°$, the highest loading is found in the lower half of the disk, i.e. in the region swept by the advancing blade. When the tilt increases to $\gamma = 90°$, the effect becomes more pronounced. Additional details can be observed from the azimuthal distributions at $r/R_{tip} = 0.75$, in Figure 9. The axial velocity component V_a varies significantly with the azimuthal angle ψ, and this variation becomes more pronounced as γ increases: a minimum is observed around $\psi \approx 100°$ and a maximum around $\psi \approx 300°$, due to the inclined inflow. The tangential component V_t shows a similar trend, but with smaller relative changes. As a result, the normalized thrust T/T_{max}

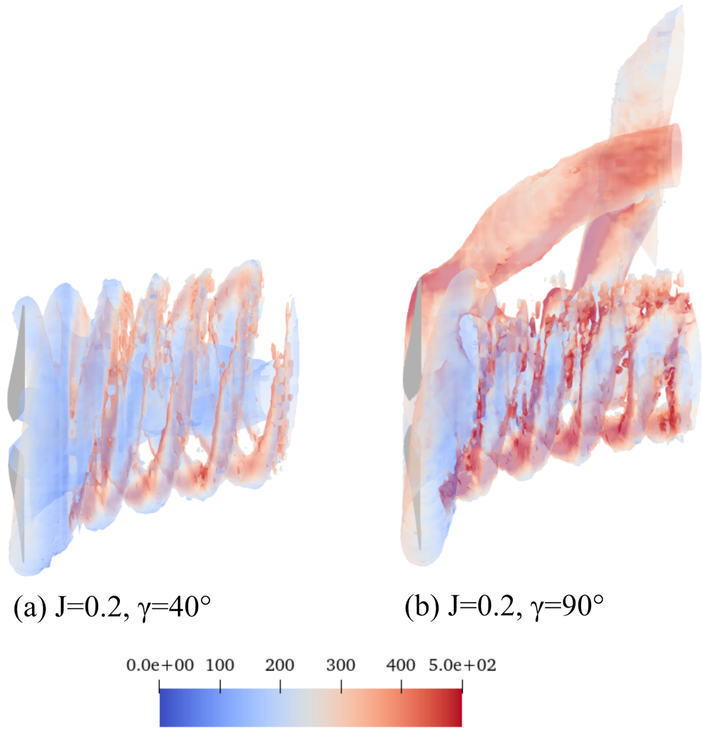

Figure 7: Propeller wake structure for different J and γ.

exhibits deeper minima and higher peaks for increasing γ, indicating a progressively more unsteady loading along the azimuth. Considering the blade element theory, the angle of attack α of each blade element (see Figure 3) can be expressed as:

$$\alpha(\psi,r) = \beta(r) - atan\left(\frac{V_a(\psi,r)}{V_t(\psi,r)}\right) \tag{5}$$

where axial and tangential velocities are defined as:

$$V_a(\psi,r) = V_{a,\infty} + v_a(\psi,r) \tag{6}$$

$$V_t(\psi,r) = \Omega \cdot r + V_{t,\infty} + v_t(\psi,r) \tag{7}$$

with v_a and v_t representing the induced velocity contributions.

From these relations, it follows that in regions of the disk where V_a is larger, the inflow angle increases and the local angle of attack decreases; conversely, lower axial velocities lead to higher α. The thrust generated by each blade element can be approximated as $T \propto W^2 C_T(\alpha)$, where $W = \sqrt{V_a^2 + V_t^2}$ is the magnitude of the relative velocity. This highlights the combined effect of both the local flow magnitude and the angle of attack in determining the sectional loading, as shown in Figure 10.

The changes in aerodynamic loading associated with the tilt angle have a direct effect on the rotor noise. As shown in Figure 11 (b), increasing γ results in higher tonal levels at the blade passing frequencies (BPFs), along with a significant rise in the high-frequency portion of the spectra.

This trend becomes more evident at higher advance ratios, as illustrated in Figure 11 (a). In particular, for $J = 0.4$, intra-harmonic components appears. These can be linked to the periodic variation of the blade loading caused by the non-uniform inflow due to the propeller tilt.

The directivity of the first BPF reflects the asymmetry introduced by both the advance ratio and the tilt angle. As shown in Figure 12, for $\gamma = 90°$, increasing the advance ratio

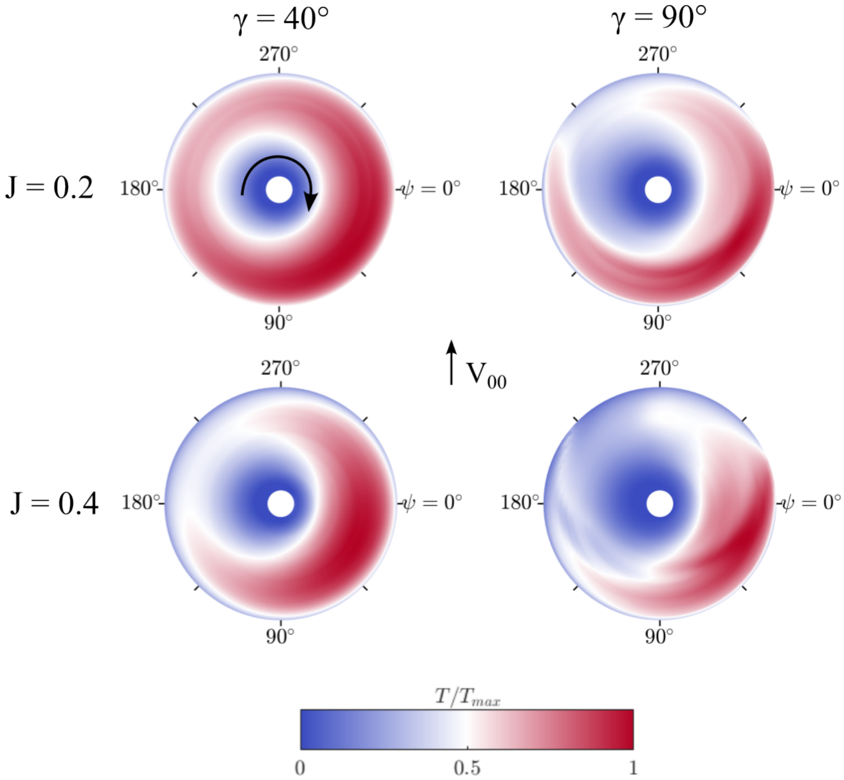

Figure 8: Adimensional thrust distribution on the propeller plane.

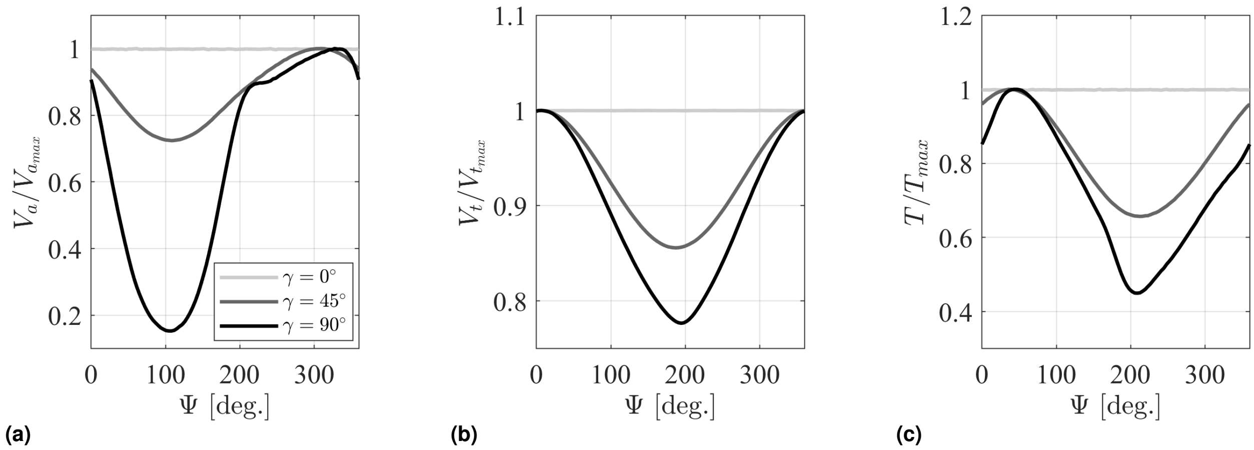

Figure 9: Azimuthal variation of axial inflow velocity V_a (a), tangential inflow velocity V_t (b) and adimensional thrust (c) at $J = 0.2$ and different γ, for a single blade element at $r/R_{tip} = 75\%$.

from $J = 0$ to $J = 0.4$ leads to a more pronounced distortion of the directivity pattern, with a clear amplification in the upstream and downstream direction. Conversely, at fixed $J = 0.2$, increasing the tilt angle progressively breaks the axisymmetric radiation typical of axial inflow. For $\gamma = 0°$, the directivity is nearly symmetric, whereas at $\gamma = 45°$ and $\gamma = 90°$ a clear lobe develops, indicating a preferential radiation direction aligned with the incoming flow.

Overall, the first BPF directivity highlights how propeller tilt and forward flight conditions lead to a strongly non-uniform acoustic field, consistent with the asymmetric loading and wake structure previously discussed.

3.2 Dynamic tilting

In this section a dynamic tilting will be analyzed. The tilting law is shown in Figure 13 and it is represented by an error function with a transient Δt of 0.1 seconds between two steady

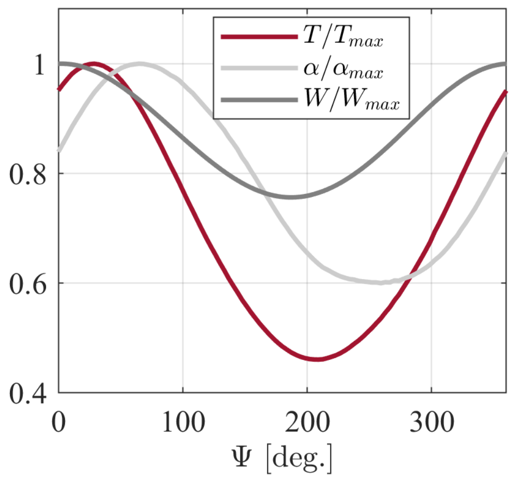

Figure 10: Azimuthal variation of normalized quantities at $J = 0.4$ and $\gamma = 45°$, for a single blade element at $r/R_{tip} = 75\%$.

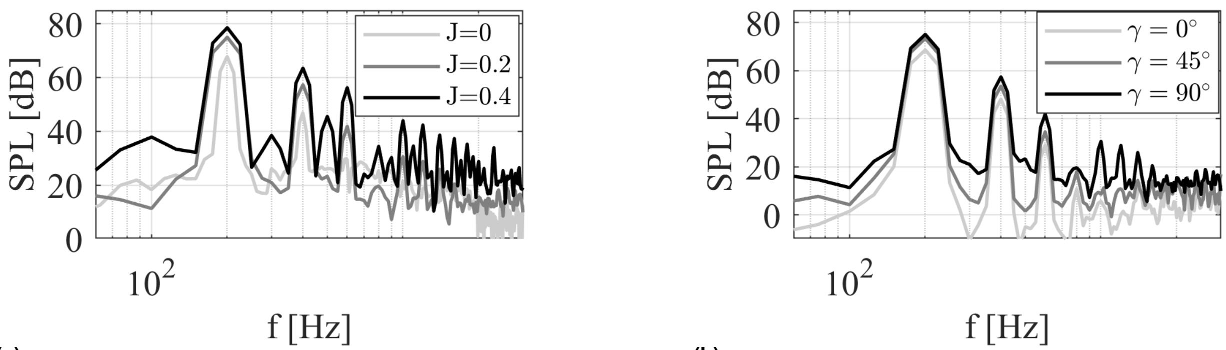

(a) (b)

Figure 11: SPL spectra for different J at $\gamma = 90°$ (a) and different γ at $J = 0.2$ (b) for an observer at $R = 10D_{prop}$ and $\theta = 270°$ (rotor plane).

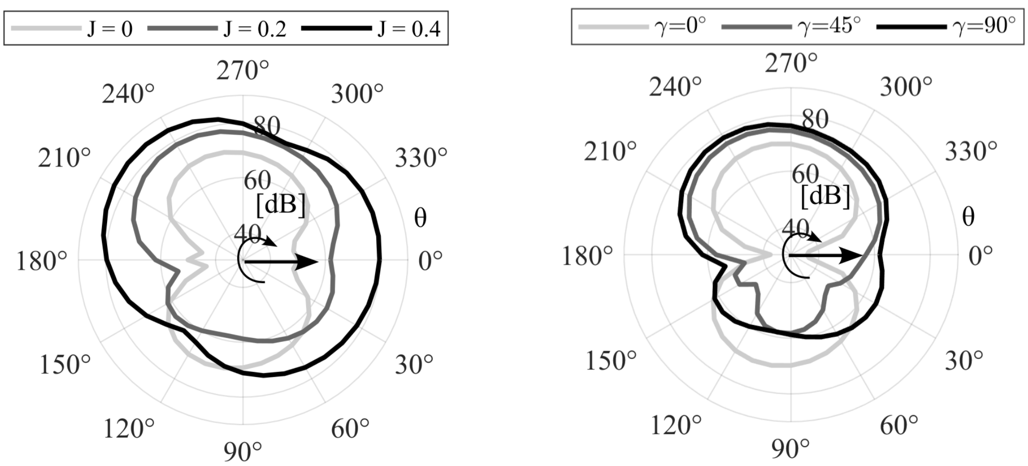

Figure 12: I BPF SPL directivity for different J at $\gamma = 90°$ (left) and different γ at $J = 0.2$ (right) for a circular mic. array at $R = 10D_{prop}$.

conditions, the first at $\gamma = 0°$ (axial inflow) and the second at $\gamma = 90°$ (crossflow) with a constant ω_x equal to 6000 rpm.

The time sequence in Figure 14 illustrates the evolution of the flow field during a dynamic tilting maneuver at $J = 0$ and $J = 0.2$, where the propeller undergoes a total rotation of $90°$. Starting from an initial condition close to axial inflow, the wake develops as a relatively coherent helical structure aligned with the rotor axis. As the tilting motion progresses, the wake is progressively deflected and stretched, losing its symmetry and becoming increasingly distorted, with regions of higher speed.

The evolution of the flow field during the tilting maneuver is reflected in the time histories of the aerodynamic coefficients reported in Figure 15. The beginning of the tilt corresponds to a clear change in both C_T and C_Q.

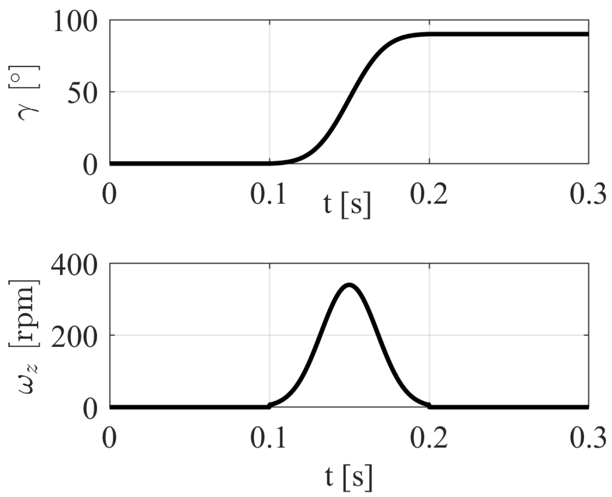

Figure 13: Tilting law.

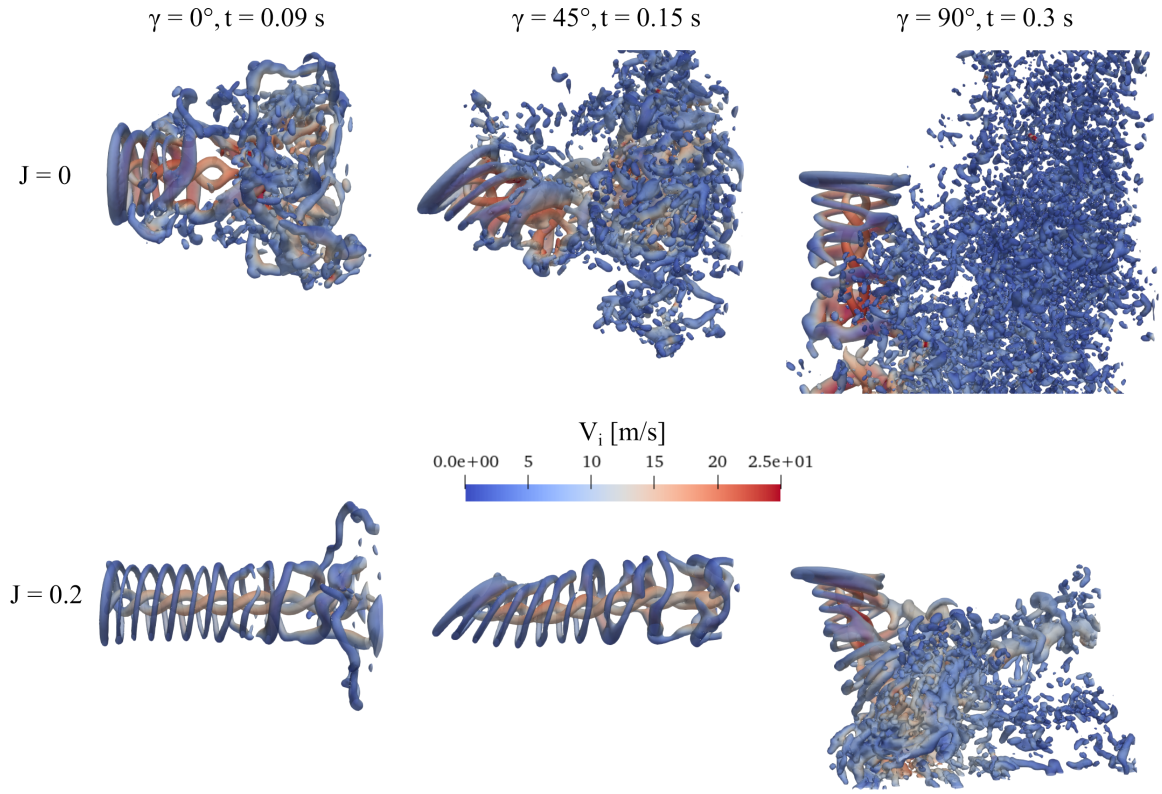

Figure 14: Propeller flowfield (induced velocity magnitude) during the transition for $J = 0$ and $J = 0.2$.

At $J = 0$, the C_T and C_Q start to oscillate as the maneuver progresses. This behavior is consistent with the progressive deformation, displacement and self-ingestion of the wake as the rotor reorients; and these oscillations persist even after the end of the transient.

When the propeller operates at $J = 0.2$, both C_T and C_Q exhibit stronger oscillations and

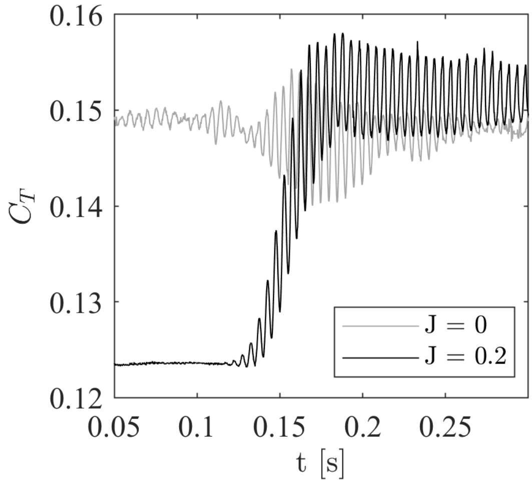

(a)

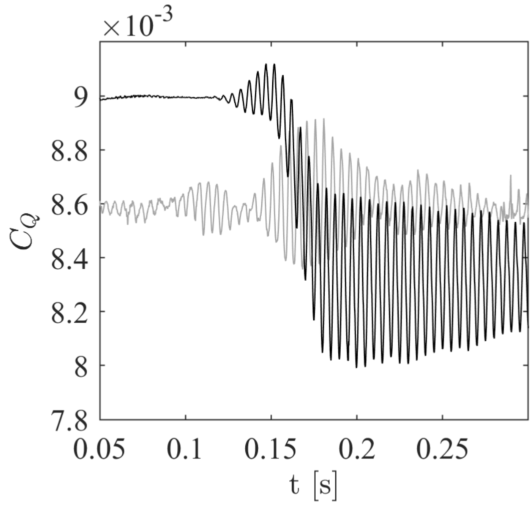

(b)

Figure 15: C_T (a) and C_Q (b) during the dynamic tilting for $J = 0$ and $J = 0.2$.

a more abrupt transition, indicating a higher level of unsteadiness. This is in agreement with the more complex wake evolution resulting from the combined effect of tilt and incoming flow.

The spanwise distributions of the unsteady thrust and tangential force fluctuations during the dynamic tilting are reported in Figure 16. For $J = 0$, both components increase during the tilting phase, showing that the attitude change alone is sufficient to introduce an unsteady aerodynamic response even in hover. Interestingly, a second increase is also visible after the maneuver, in the nominally steady post-tilt condition. This suggests that, although the rotor kinematics become steady after $t = 0.2$ s, the wake does not immediately adapt to the new orientation. The blades therefore continue to interact with a distorted inflow field generated during the tilting motion.

When the advance ratio is increased to $J = 0.2$, the fluctuations become much stronger and more coherent in time. The alternating positive and negative bands indicate a periodic modulation of the sectional thrust and tangential force, mainly concentrated over the outer part of the blade. This behavior is attributed to the combined effect of the tilting motion and the skewed inflow, which breaks the axial symmetry of the rotor wake and produces stronger azimuthal variations of the blade loading.

The SPL hemispheres in Figure 17 show how both the tilt angle and the advance ratio affect the radiation pattern. At $J = 0$, the case with $\gamma = 0°$ presents a relatively dipolar shape of the SPL distribution over the sphere. When the tilt angle increases to $\gamma = 45°$, the sound field becomes more evenly distributed and higher in level. At $\gamma = 90°$, the pattern changes, with a distinct low SPL region appearing below the rotor, indicating that the acoustic energy is being redistributed.

At J=0.2, the effect of the tilt is more evident. As γ increases, higher SPL levels are observed over a larger portion of the sphere. In particular, at $\gamma = 90°$, the radiation becomes clearly directional, with a high SPL region concentrated on the advancing side and a lower level on the opposite side.

Figure 18 reports the time evolution of the OASPL at different observer positions during the tilting. At $\psi = 0°$, the overall increase in sound level is accompanied by noticeable overshoots and undershoots, particularly for J=0. These fluctuations appear around the onset of the tilt and reflect the rapid change in the acoustic emission as the rotor departs from its initial configuration. A similar behavior is observed at $\psi = 20°$, where the transient is even more evident, with pronounced peaks and dips before the signal settles to a higher level. At $\psi = 90°$, these effects are less marked, although a mild overshoot can still be identified for $J = 0.2$. In contrast, the $J = 0$ case remains relatively smooth across all observer positions.

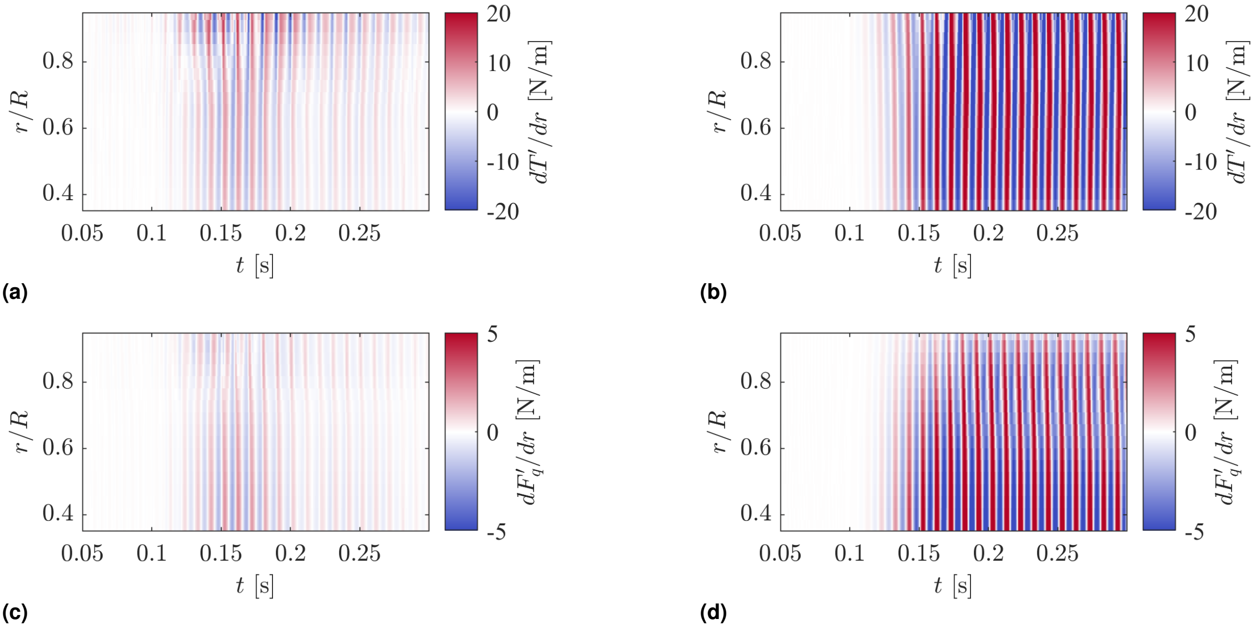

Figure 16: Spanwise distribution of unsteady thrust and tangential force fluctuations during the dynamic tilting for $J = 0$ (a, c) and $J = 0.2$ (b, d).

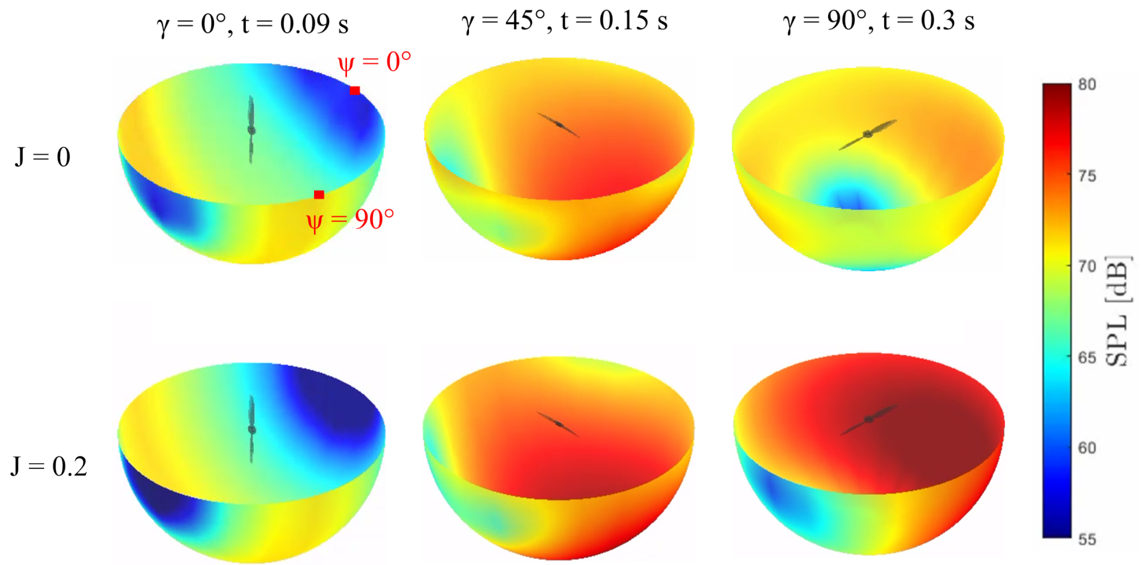

Figure 17: SPL hemispheres for $J = 0$ and $J = 0.2$ during the dynamic tilting.

The overshoots and undershoots observed in the OASPL signals can be related to the time–frequency content shown in Figure 19. During the tilting phase, the acoustic energy is not steady but appears in short time intervals, especially at $\psi = 20^\circ$, where a clear high-frequency contribution is visible. For J=0, the spectrogram shows a moderate increase of energy during the tilting, which then disappears once the tilting is completed. In the case J=0.2, the same region is characterized by stronger and more structured activity, with tonal components appearing over a wider frequency range. This behavior is consistent with the larger oscillations and the more pronounced peaks observed in the OASPL. At $\psi = 90^\circ$, the energy remains confined at low frequencies and varies only slightly in time. As a result, the corresponding OASPL signals are smoother and do not show significant overshoot or undershoot.

Considering high-order metrics (Tinney & Valdez, 2024), such as kurtosis k, skewness γ, number of zero crossing per rotation N_z/rev and quadrature spectral density Q_{sum} for the

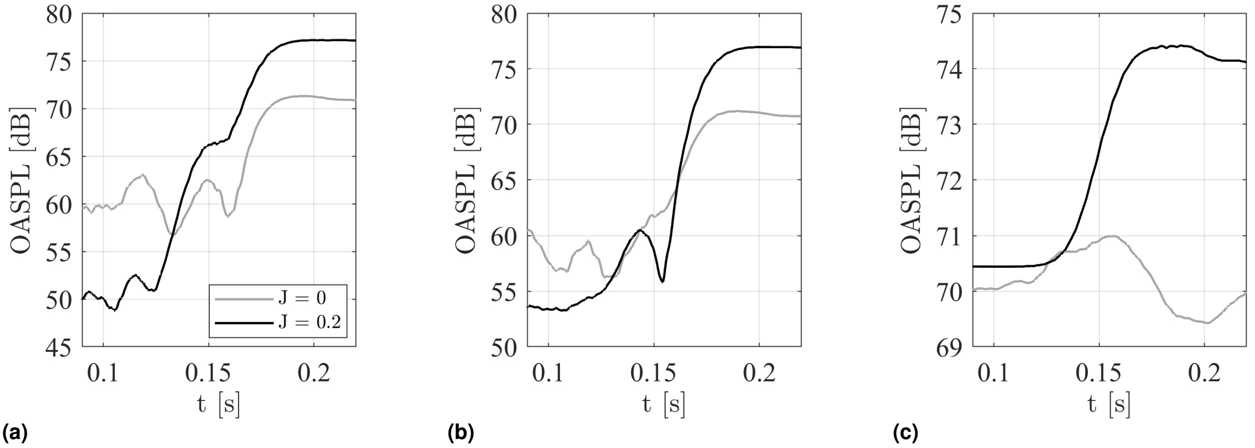

Figure 18: OASPL for $\psi = 0°$ (a), $\psi = 20°$ (b) and $\psi = 90°$ (c) at $J = 0$ and $J = 0.2$ during the dynamic tilting.

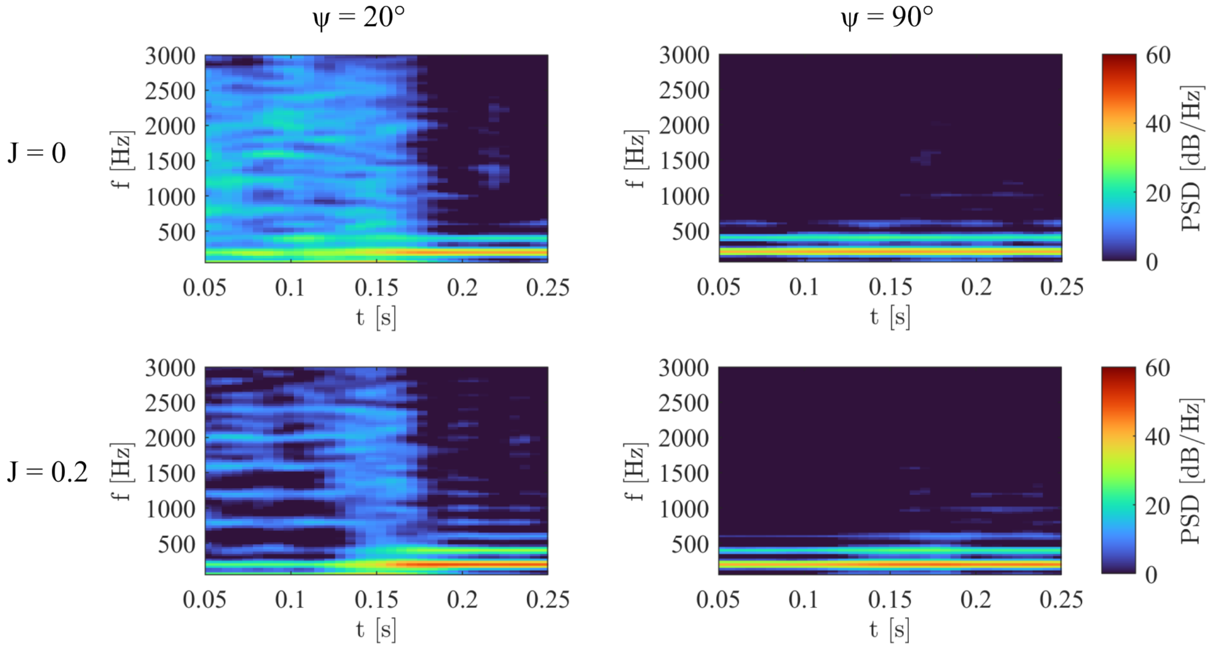

Figure 19: Spectrograms of the dynamic tilting for $\psi = 20°$ and $\psi = 90°$, for $J = 0$ and $J = 0.2$.

acoustic pressure and its time derivative, help to better characterize the changes during the tilting operation.

Kurtosis, defined as $k(p) = \langle p^4 \rangle / \sigma_p^4$, is a measure of waveform peakedness. For $k > 3$ is said to have a heavy-tailed distribution, while for $k < 3$ the distribution is narrow, while the skewness $\gamma(p) = \langle p^3 \rangle / \sigma_p^3$ is a measure of wave symmetry and it is 0 for a symmetric distribution. Finally, the number of zero crossing per revolution refers to the number of times in which the waveform flip sign, and $Q_{\text{sum}} = \int_0^\infty f S_{pp}(f) df$, where S_{pp} is the power spectral density of the pressure signal.

For observers close to the rotor axis, both kurtosis and skewness show clear peaks during the transient, indicating that the pressure signal becomes not only more peaked but also asymmetric. This effect is essentially absent for the in-plane observer ($\psi = 90°$), highlighting the strong directional dependence of the phenomenon.

At the same time, the decrease in the zero crossing rate indicates that this distortion is not due to an increase in oscillatory activity, but rather to a temporary change in the waveform shape.

The effect becomes more pronounced at higher advance ratio. In the $J = 0.2$ case, the

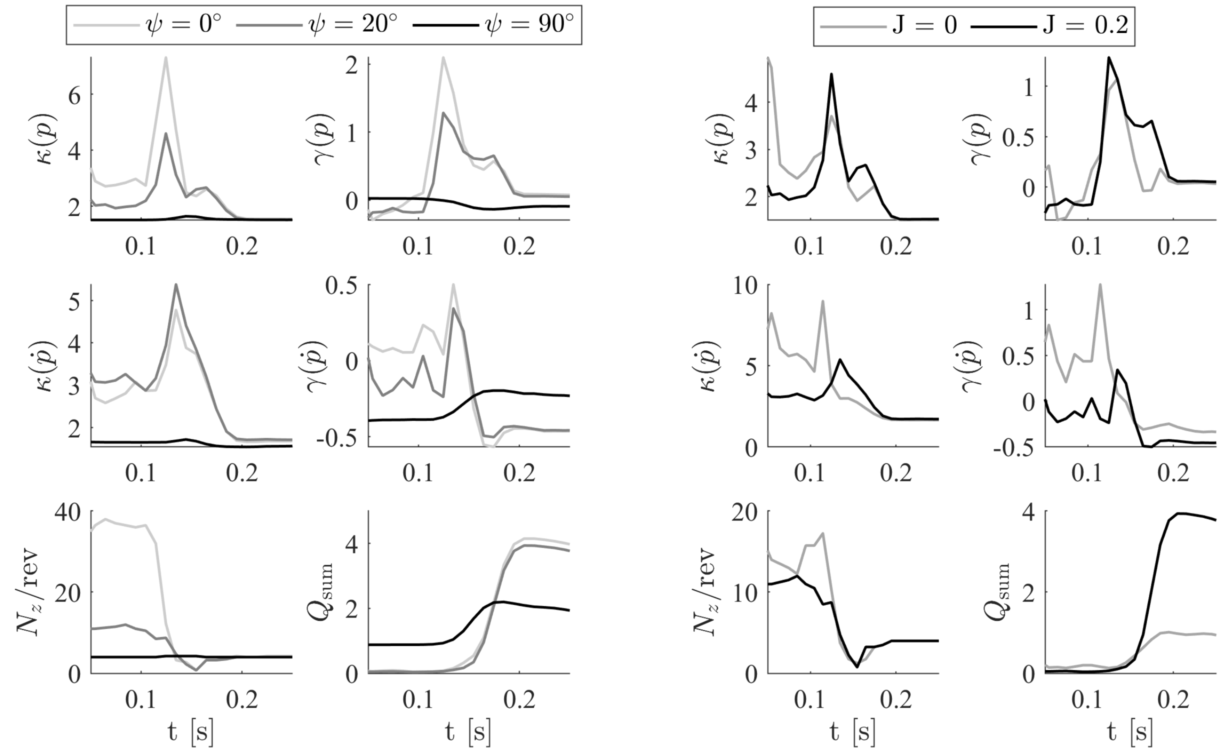

(a) (b)

Figure 20: High-order metrics for different ψ and $J = 0.2$ (a) and $\psi = 20°$ for different J (b).

skewness reaches larger values and the quadrature spectral density increases more significantly. This suggests that forward flight enhance both the asymmetry of the signal and the redistribution of energy towards higher frequencies, likely as a result of stronger loading asymmetry.

4. Conclusions

In this work, the noise generated by a tilting propeller has been investigated under both static and dynamic conditions. The analysis highlights that the tilting motion introduces strong unsteady effects that cannot be described as a simple sequence of steady states. From an aerodynamic perspective, the tilting maneuver leads to a progressive distortion of the wake, with loss of symmetry and increased interaction between the rotor and its own induced flow. This results in significant variations of the blade loading.

These effects are directly reflected in the acoustic field. Compared to fixed tilting angle conditions, dynamic tilting produces a time-dependent redistribution of acoustic energy, with noticeable changes in both magnitude and directivity. In particular, the OASPL exhibit overshoots and undershoots during the transient, which are associated with the rapid variation of the loading and the non-stationary nature of the wake. The spectrogram analysis confirms that these features are linked to the appearance of localized acoustic energy in time and frequency, especially at off-axis observer positions. The effect becomes more pronounced at higher advance ratios, where the interaction between tilt and inflow enhances both the asymmetry of the loading and the high-frequency content of the radiated noise.

Overall, the results indicate that dynamic tilting cannot be accurately captured by quasi-steady approaches, and that transient effects play a key role in determining the aeroacoustic signature of the propeller.

Future work will focus on extending the analysis to more complex maneuvers and on assessing the impact of different tilting rates and operating conditions.

Acknowledgments

This work is part of the project PNRR-NGEU which has received funding from the MUR-DM 117/2023 and is co-funded by the Italian Aerospace Research Center (CIRA).

References

Alvarez, E. J., & Ning, A. (2018). Development of a vortex particle code for the modeling of wake interaction in distributed propulsion. In *2018 applied aerodynamics conference.* AIAA. doi: 10.2514/6.2018-3646

Alì, M., Piccolo, A., Zamponi, R., Ragni, D., & Avallone, F. (2026). On the aeroacoustics of a propeller at low reynolds number subjected to a grid-induced turbulent inflow. *Aerospace Science and Technology*, *176*, 112114. doi: https://doi.org/10.1016/j.ast.2026.112114

Brentner, K. S., & Farassat, F. (2003). Modeling aerodynamically generated sound of helicopter rotors. *Progress in Aerospace Sciences*, *39*, 83–120. doi: 10.1016/S0376-0421(02)00068-4

Bres, G. A., Brentner, K. S., Perez, G., & Jones, H. E. (2004). Maneuvering rotorcraft noise prediction. *Journal of Sound and Vibration*, *275*, 719–738. doi: 10.1016/j.jsv.2003.07.005

Chen, H. N., Brentner, K. S., Lopes, L. V., & Horn, J. F. (2006). An initial analysis of transient noise in rotorcraft maneuvering flight. *International Journal of Aeroacoustics*, *5*, 109–138. doi: 10.1260/147547206777629853

Glegg, S., & Devenport, W. (2017). Aeroacoustics of low mach number flows. Academic Press.

Hasan, S. (2018). *Urban air mobility (uam) market study* (Tech. Rep.). NASA.

Jamaluddin, S., N, Celik, A., Baskaran, K., Rezgui, D., & Azarpeyvand, M. (2024). Aerodynamic noise analysis of tilting rotor in edgewise flow conditions. *Journal of Sound and Vibration*, *582*. doi: https://doi.org/10.1016/j.jsv.2024.118423

Picillo, M., Barbarino, M., & Avallone, F. (2026). Low-fidelity methodology for rotor tonal noise prediction during angular velocity transients. *AIAA Journal*, *0*(0), 1-12. doi: 10.2514/1.J066745

Romani, G., Grande, E., Avallone, F., Ragni, D., & Casalino, D. (2022). Computational study of flow incidence effects on the aeroacoustics of low blade-tip mach number propellers. *Aerospace Science and Technology*, *120*. doi: 10.1016/j.ast.2021.107275

Ryll, M., Bülthoff, H. H., & Giordano, P. R. (2012). Modeling and control of a quadrotor uav with tilting propellers. In *2012 ieee international conference on robotics and automation* (p. 4606-4613). doi: 10.1109/ICRA.2012.6225129

Son, S. M., Song, C.-H., Araghizadeh, M. S., Myong, R. S., & Lee, H. (2025, 10). Investigation of aerodynamics, wake dynamics, and aeroacoustic characteristics of a full-configuration tiltrotor aircraft during transition flight. *Physics of Fluids*, *37*(10), 107133. doi: 10.1063/5.0296874

Tinney, C. E., & Valdez, J. A. (2024). Higher-order statistical metrics for characterizing multirotor acoustics. *AIAA Journal*, *62*(11), 4431–4441. doi: 10.2514/1.J064032

Voropayev, V., Marques, M., Maleki, A., Grace, S., Lyrintzis, A. S., Mankbadi, R. R., & Golubev, V. V. (2025). High-fidelity simulations of vertiport gust effects on evtol rotor noise. In *Aiaa aviation forum.* AIAA. doi: https://doi.org/10.2514/6.2025-3001

Wang, Z., Bi, Y., Wu, H., & Zhong, S. (2026). Prediction of the tonal noise of rotors in transition flight. In *32nd aiaa/ceas aeroacoustics conference (2026).* doi: 10.2514/6.2026-3345

Zanotti, A., Velo, A., Pepe, C., Savino, A., Grassi, D., & Riccobene, L. (2024). Aerodynamic interaction between tandem propellers in evtol transition flight configurations. *Aerospace Science and Technology*, *147*, 109017. doi: https://doi.org/10.1016/j.ast.2024.109017

Zhou, Y., Zhao, H., & Liu, Y. (2020). An evaluative review of the vtol technologies for unmanned and manned aerial vehicles. *Computer Communications*, *149*, 356–369. doi: 10.1016/j.comcom.2019.10.016